# Environmental significance of kaolinite variability over the last centuries in crater lake sediments from Central Mexico

Nathalie Fagel[1], Isabel Israde-Alcantara[2], Reza Safaierad[1], Marttiina Rantala[1], Sabine Schmidt[3], Gilles Lepoint[4], Pierre Pellenard[5], Nadine Mattielli[6] and Sarah Metcalfe[7]

*1. AGEs, Department of Geology, Université de Liège, Belgium, nathalie.fagel@uliege.be.*

*2. Instituto de Investigaciones en Ciencias de la Tierra, Universidad Michoacana de San Nicolás de Hidalgo. Morelia, Michoacán, México*

*3. Univ. Bordeaux, CNRS, Bordeaux INP, EPOC, UMR 5805, F-33600 Pessac, France*

*4. LETIS, Université de Liège, Belgium*

*5. Biogéosciences UMR 6282 CNRS/ub/EPHE, University of Burgundy, Dijon, France*

*6.G-Time, Université Libre de Bruxelles, Belgium*

*7. School of Geography, University of Nottingham, Nottingham NG7 2RD, United Kingdom*

## Abstract (239 words)

Environmental conditions have a notable impact on clay minerals, primarily because of the chemical reactions they undergo with their immediate environment. These reactions are more pronounced in hot and humid tropical regions, and therefore, the study of clays deposited at the bottom of lakes in tropical regions can yield valuable insight into past environmental conditions. Here we present multiproxy records, including physical (magnetic susceptibility, grey-scale level and grain size), mineralogical (X-ray diffraction, Simultaneous Thermal Analysis, Fourier-Transform Infrared Spectroscopy), and geochemical (elemental composition by XRF-core scanner, organic geochemistry by IRMS) data, from three 210Pb-dated sediment cores (spanning recent centuries < CE 1470) retrieved from crater lakes Los Espinos, Tacámbaro and Teremendo in the Trans-Mexican

Volcanic Belt (TMVB), central Mexico. The mineralogical results showed that disordered kaolinite, formed by hydrolysis and hydrothermal alteration, was the predominant mineral in the sediments of the three lakes. The abundance of kaolinite changed in line with organic carbon and organic matter-related elements (Br, S and Ni) and showed opposite trends with lithogenic elements (Ti, K, and Fe). The geochemical data further suggested that increases in kaolinite abundance are linked to the formation of organo-mineral aggregates related to periods of elevated lake productivity that in turn may reflect lake level changes in the closed basins. In Lake Tacámbaro, following the construction of a canal in the early 20th century and subsequent regulation of lake level, the relationship between organic material and kaolinite was no longer present.

Keywords: XRD Mineralogy; XRF-core scanner; Runoff; Hydrolysis; Tropics; Late Holocene

## 1. Introduction

Central Mexico (Figure 1) is a suitable area to study climate variability as it lies beyond the northern limit of the Intertropical Convergence Zone (ITCZ) (Barron et al., 2012), and near the southern limit of the area influenced by the North American Monsoon (NAM) (Douglas et al., 1993; Higgins et al., 1999) which, together with convective storms, brings a summer dominated rainfall regime to the area. NAM rainfall is modulated by the El Nino Southern Oscillation (ENSO), with generally reduced/increased summer precipitation during El Niño/La Niña events (Castro et al., 2001). ENSO is a pseudo-periodic climate pattern involving variations in sea surface temperatures and winds over the eastern tropical Pacific (McPhaden et al., 2006).

The selected study area, i.e. the Trans Mexican Volcanic Belt (TMVB), has widespread crater lakes that are closed systems that may record climatic variability in their sedimentary sequences with relatively limited influence of direct human impact (Alcocer et al., 2000; Cobb et al., 2013). In crater lakes, the lake level is mainly controlled by the water balance between evaporation and precipitation (Gomez-Tagle Chavez et al., 2002). Direct anthropogenic perturbations in the TVMB with an impact on lake water level are recent. In fact, the sharp decrease in the water level of some lakes observed since the 1970s has been explained by the over-exploitation of groundwater for irrigation and urban purposes (Alcocer et al., 2000), which has led to the complete drying of some crater lakes such as La Alberca in 2006 (Kienel et al., 2009) and la Hoya Rincon de Parangueo (Park et al., 2019).

In the TMVB area, previous paleolimnological studies have focused on deep (≥ 30 m) and/or large lakes with records of climate variability over the last 30 kyr (La Piscina de Yuriria) (Holmes et al., 2016) to 48 kyr (Pátzacuaro) (Bradbury, 2000). Additionally, only a limited number of laminated sediments with millennial and decadal resolution have been recovered. In Lake Tacámbaro, for example, a Holocene sequence (9.4 kyr BP to 1760 CE) is mainly laminated but the uppermost sediment (~190 yr) was lost during coring (Ortega-Guerrero et al., 2021). A centennial to decadal resolved paleoclimatic record for the last 6.7 kyr BP was retrieved from a partly laminated sedimentary sequence from the La Alberca maar lake (Wogau et al., 2019). Short cores from this lake and lake Hoya Rincón de Parangueo, both located in Valle de Santiago, reveal varved sediments for the periods 1852-1973 and 1839-1943 CE, respectively (Kienel et al., 2009). These varved sediments consist of light coloured authigenic carbonate-rich laminae formed by a supersaturated water column during the dry season and dark-coloured detrital laminae formed by surface runoff during the wet season. Although some relationship was observed between detrital sedimentation and local precipitation, it was not significant (Kienel et al., 2009).

77 Lakes are sensitive sensors of environmental and climatic changes (e.g. Adrian et al.,
78 2009), mainly influenced by seasonal temperature and precipitation regimes. In Central
79 Mexico, the increase of temperature starting in spring (Figure 1) favours stable stratification
80 of the upper water column leading to a progressive nutrient limitation in summer, followed by
81 water column mixing in winter (Winder et al., 2009). Such thermal control is manifested, for
82 example, by changes in phytoplankton assemblages in Lake Tacámbaro (Caballero et al.,
83 2016). Rainfall induces surface runoff which carries both organic and mineral detritus into the
84 lake (Kienel et al., 2009). In tropical lakes, spring algal blooms are related to increased
85 temperature, but also nutrients washed into the lake by rainfall (Lind et al., 1992). In summer,
86 the intense rainfall increases water turbidity and dilutes nutrients in the stratified upper water
87 column, leading to a reduction in biological productivity (Gomez-Tagle Chavez et al., 2002).
88 Among other meteorological forcings, the impact of wind action on thermal stratification is
89 limited in crater lakes due to their low surface/depth ratio and steep crater walls (Kienel et al.,
90 2009; Briddon et al., 2023).

91 The mineralogy of crater lake sediments may be used as a reliable proxy for the degree
92 of chemical weathering and physical erosion of the crater soil cover, which in turn reflects
93 the climatic conditions within the closed watershed. Among the detrital minerals, clay
94 minerals are formed in the upper soil profile by the weathering of parent rocks (Pedro, 1968;
95 Singer, 1984; Warr, 2022). Their mineralogy reflects the degree of physical decomposition
96 and chemical transformation during pedogenetic processes (Chamley, 1989; Weaver, 1989).
97 Under a warm and humid tropical climate, the intense hydrolysis of primary minerals leads to
98 a complete leaching of cations and partial removal of silica (*i.e.* monosialitisation process).
99 The secondary clay mineral formed, i.e. kaolinite [$Al_2Si_2O_5(OH)_4$], is a combination of a layer
100 of aluminium with a layer of silica (1:1 clay mineral). A stronger hydrolysis leads to a
101 complete leaching of the silica and allows the formation of silica-free secondary phases such

as gibbsite [$Al(OH)_3$], boehmite [AlO(OH)] or diaspore [AlOOH] in association with other immobile elements such as iron (Saalfeld and Wedde, 1974). In addition to climate, the topography and lithology of the parental rock also control clay formation (Singer, 1984). For instance, the volcanic rocks that constitute the parental rock of the crater flanks are more sensitive to weathering than other crystalline rocks. However, according to Chamley (1989), climate remains the most important influencing factor under strongly hydrolysing conditions.

The aim of this study is to compare mineralogical and geochemical proxies of three sedimentary cores retrieved from Central Mexico in order to explore the main environmental factors controlling the sedimentary cycle, from alteration processes and erosion to lacustrine sedimentation, over the past centuries. Particular emphasis is given to the evolution and significance of the relative abundance of kaolinite in the sedimentary records.

## 2. Study area

Sediment cores were collected from three crater lakes in the Michoacán-Guanajuato volcanic field, in central part of the TMVB (Figure 1A and 1B). The TMVB is an active volcanic arc, located between ~18°30'N and 21°30'N, related to the oblique subduction of the Cocos Plate beneath the North American Plate (Ferrari et al., 2012). The studied lakes in the TMVB constitute promising sites for high-resolution paleolimnological studies (Figure 1C). These lakes correspond to "maars" that originated by phreatomagmatic eruptions (Cifuentes and Fucugauchi, 1999) and range in altitude from 1475 to 2058 masl.

Based on meteorological data (30-year average: 1981-2010) from three stations near the lakes (Figure 1D), the mean monthly temperature in Tacámbaro ranges from 17 to 22°C (annual average 19°C) while the temperatures are slightly cooler in Teremendo ($14 \leq T \leq 20$°C) and Villa Jimenez (i.e. the station located 2 km NE of Lake Los Espinos, $13 \leq T \leq 21$°C). More than 92% of the annual precipitation falls in summer, from late May to October

(Figure 1B). Tacámbaro is characterized by the highest mean annual precipitation of 1168 mm/yr. Teremendo is the driest location with 700 mm/yr, whereas Villa Jimenez station displays intermediate values with 896 mm/yr.

[Insert Figure 1]

Los Espinos crater (19°54'25" N, 101°46'06" W, 1940 masl - Figure 1C) is a well-preserved tuff volcanic cone located on the north-western margin of the Zacapu tectonic lacustrine basin (Hasenaka and Carmichael, 1985). Its formation dates back to 25 kyr BP. Its basement consists of basalts and andesites, which are hosted in granitic rocks (Sigala et al., 2017). The crater has an elliptical shape (0.33 $km^2$) with a NE-SW orientation and accommodates a lake of 350 m in diameter (area 0.1 $km^2$) with a maximum depth of 30 m (Siebe et al., 2012). The water column is mixed in winter (December-February) but stratified during the rest of the year (Hernández-Morales et al., 2011). The chlorophyll a ranges between 0.5 and 1.5 $mg/m^3$. The inner slopes of the crater are vegetated with tropical deciduous and gallery forests, helping to reduce the movement of sediments downslope into the lake.

The Tacámbaro crater (19°12'38" N, 101°27'33" W, 1475 masl - Figure 1C) was formed during the Pliocene (Guilbaud et al., 2012). Its volcanic basement is made of basalts and dacites whereas the youngest < 1 Ma volcanic rocks are andesite and basaltic andesites (Guilbaud et al., 2012). In this location, the host rocks are made of siliciclastic and carbonate rocks (Sigala et al., 2017). The crater is characterized by steep walls (28 m) and narrow shore zones, except on its eastern flank (Ortega-Guerrero et al., 2021). The lake is small with a diameter of 300 m (surface area 0.08 $km^2$) and a maximum depth of 28 m (Caballero et al., 2016; Sigala et al., 2017). The lake was a closed system until the construction of a canal at the beginning of the 20th century to regulate the lake depth (Ortega-Guerrero et al., 2021). The lake type is warm monomictic, yearly stratified except in January (Hernández-Morales, 2011).

It is characterized by eutrophic conditions with annual maximum chlorophyll a concentrations ranging from 25 to 75 mg/m$^3$ (Sigala et al., 2017). The vegetation of the crater is diverse, ranging from a typical temperate forest to a low deciduous forest (Morales et al., 2008).

The Teremendo crater (0.65 km$^2$), formed during the Pliocene, has steep walls made of basalts and andesites overlying granitic basement (Soria-Caballero et al., 2019). The crater lake (19°48'25" N, 101°27'15" W, 2058 masl - Figure 1C) is shallow (depth ≤ 9 m) (Sigala et al., 2017) and covers an area of 0.15 km$^2$ with a circular shape. The lake stratifies from March to November and is hypertrophic with an annual chlorophyll a concentration of ≥ 75 mg/m$^3$ (Sigala et al., 2017). Based on field observations, the crater is covered by a seasonal dry forest, which has been partially deforested and replaced by cattle pasture and shrubland. Additionally, the marginal areas of the lake are colonized by (semi-)aquatic plants.

## 3. Material and methods

### 3.1. Sedimentological analyses

In June 2019, three crater lakes in Central Mexico were sampled using a Uwitec® gravity corer, with a 9 cm core barrel. Cores were retrieved in the central part of each lake, namely LLEs19-2 (53 cm, water depth 30 m) from Lake Los Espinos, LTa19-3 (93.5 cm, water depth 26 m) from Lake Tacámbaro and LTe19-4 (109 cm, water depth 8 m) from Lake Teremendo (Figure 1B & 1C). After the fieldtrip, the three cores were split lengthwise, described and photographed. Before transport, one half-core section was subsampled in one or two contiguous 4 cm wide rectangular plastic tubes ≤ 74 cm long for non-destructive analyses and into 25 cm long x 4 cm wide x 1.5 cm deep aluminium boxes for destructive analyses. The second half-core section was stored at 4°C for diatom and pollen analyses.

The subsamples within the plastic channels were scanned for physical (grayscale image, magnetic susceptibility) and X-ray Fluorescence (XRF) geochemical characterization of the

177 sediment. Magnetic susceptibility (MS) of the sediment was measured at 5 mm intervals using
178 a Bartington® instrument MS2E point sensor, following the protocol described in Bartington-
179 Instruments (2008). Three measurements expressed in SI units, equivalent to $10^{-6}$ CGS, were
180 averaged to obtain a representative profile (AGEs, Belgium). A SCOPIX X-ray image-
181 processing system (EPOC, University of Bordeaux, France) was used at 58 kV, 10 mA and a
182 step size of 15 μm to determine the grayscale image of the sediment cores (Migeon et al.,
183 1998).

184 Wet bulk density was calculated by weighing 1 $cm^3$ of wet sediment at 1 cm intervals for
185 the top 25 cm of the cores. Grain-size analyses were done with a sampling resolution of 4 to 5
186 cm using a Malvern® Mastersizer 2000 laser diffraction particle analyser (ARGENCO,
187 University of Liège, Belgium). Each bulk sediment sample was dispersed in deionised water,
188 sieved to 2 mm and introduced into the dispersion unit cell (Hydro 2000G). The sample
189 volume was adjusted to reach a laser beam obscuration of 10±5%. Before analysis, the sample
190 was homogenised using a 2000 rpm stirrer and disaggregated using moderate ultrasonic
191 waves (i.e. 2.6 W power). An average of three measurements was calculated for data
192 reproducibility. The relative abundance of clay (i.e. < 2 μm), silt (2-63 μm) and sand (>
193 63 μm) fractions was calculated for each sample. The silt fraction was subdivided into fine (2-
194 10 μm), medium (10-30 μm) and coarse silt (30-63 μm) fractions.

195 Mineralogical analysis was performed by X-ray diffraction (XRD) using a Bruker® D8-
196 Advance Eco diffractometer (CuKα radiance, λ=1.5418Å, 40 KV, 25 mA) coupled with a
197 Lynxeye XE detector (AGEs, University of Liège). The sampling resolution reaches up to 1
198 cm for LTa19-3 (n=72) and 4 to 5 cm for LLEs19-3 (n=10) and LTe19-4 (n=22). The dried
199 (40°C) bulk sediment sample was ground by hand with an agate mortar. The powder was
200 sieved at < 150 μm and transferred to a plastic holder using the backside method (Moore and

201 Reynolds, 1989) and scanned from 2 to 70° 2θ with a step size of 0.009°2θ and 0.5 seconds
202 per step. Mineral identification and quantification were done using the EVA and TOPAS ®
203 Bruker software, respectively. A Rietveld refinement was applied to all the minerals identified
204 by XRD (Rietveld, 1967; Brindley, 1980b; Bish, 1993a; Środoń, 2002). Preferred orientations
205 and unit cell parameters of the mineral phases were progressively adjusted to obtain a
206 reconstructed XRD pattern as close as possible to the measured pattern.

207 To complement the XRD analysis, a Simultaneous Thermal Analyser (STA, Mettler-
208 Toledo® STAR$^{e}$ System) was used to follow the origin and transformation processes of the
209 clay minerals through the sedimentary cycle. STA allows the degree of order-disorder of
210 individual clay minerals to be estimated, giving clues on their origin and transformation
211 processes (e.g. Patterson and Swaffield, 1987; Hemminger and Cammenga, 1989; Emmerich,
212 2010). Thermal analysis also provides information on the presence of disordered (Smykatz,
213 1974; Drits et al., 1995) and/or amorphous mineral phases, even at low abundances
214 (Emmerich, 2010). The presence of these phases, which remain largely undetected in the
215 XRD analysis, is indicative of mineral transformation and/or dissolution occurring in specific
216 environmental conditions (e.g. pedogenesis, weathering). STA analysis was made on bulk
217 sediment powder on a selection of 12 samples from the 3 cores characterized by variable
218 proportions of kaolinite (AGEs, University of Liège). The sample weight loss
219 (Thermogravimetric TG curve) and associated heat exchanges (Differential Scanning
220 Calorimetry DSC curve) were followed at a constant heating rate of 20°C per minute from 25
221 to 1200°C under a nitrogen atmosphere (80 ml/min). The first derivative of the
222 thermogravimetric curve (DTG) represents the rate of weight loss. It was calculated since
223 DTG peak gives the specific temperatures characteristic of the different mineral components
224 more accurately than the TG curve and indicates the characteristic temperature of the
225 reactions occurring in the samples (Földvári, 2011), in particular dehydration and

dehydroxylation for clay minerals. The STA data were processed using the evaluation software Metler Toledo STAR$^{e}$ SW16.40.

Fourier Transform Infrared Spectroscopy (FTIR) was carried out on 8 samples already analyzed by STA using a Nicolet NEXUS Spectrometer (Laboratory of Mineralogy, University of Liège). Pellets were made from 2 mg of powdered sample, ground to < 250 µm and 148 mg of potassium bromide. The measurement was made in the range of 4000 to 400 $cm^{-1}$ with a resolution of 1 $cm^{-1}$. FTIR is a method commonly used to assess the degree of disorder (Lorentz et al., 2018).

Scanning Electron Microscope (SEM) imaging was carried out at the University of Burgundy (ARCEN analytical platform) on 6 samples using a Hitachi SU8230, with a resolution of 0.8 nm (15kV, WD = 4 mm), equipped with a ThermoFisher Scientific UltraDry 30 $mm^2$ Energy Dispersive X-ray (EDS, 127 eV Mn energetic resolution) in order to comfort XRD and geochemical analyses. Sieved sediments at 30 µm were used for observations after aqueous suspension of the sediment on a SEM spinner covered with copper tape and hydrophilization under air plasma in primary vacuum.

An Avaatech XRF core scanner (EPOC, University of Bordeaux, France) equipped with a Fe-Mo tube was used with a step size of 1 mm to characterize the bulk sediment geochemistry (e.g. Frugone-Álvarez et al., 2017). Measurements of fourteen elements (i.e. Al, Si, S, K, Ca, Ti, Mn, Fe, Co, Ni, Br, Sr, Zr and Pb) were done with voltages of 10, 30 and 50 kV and counting times of 15, 20 and 25 seconds, respectively. Semi-quantitative concentration profiles of the elements were plotted through the depth of the sediment core based on the variation of their peak areas measured on XRF spectra and expressed as counts per second (cps). A statistical approach was applied to the XRF dataset using version 4.2.2 of the R environment (R Development Core Team, 2013). First, the XRF count data were transformed to centred log-ratio (clr) using *rgr* package (Garrett and Garrett, 2018). A Robust Principal

Component Analysis (RPCA, Candès et al., 2011) was then applied to the clr data using the package *pcaPP* (Filzmoser et al., 2018) as proposed by Żarczyński et al. (2019). The 14 elements were included in the analysis. The principal components (PC) with an eigenvalue > 1 were retained as significant for the total variance of the dataset (Davis, 2002).

Sediment organic geochemistry, including organic carbon (C) and nitrogen (N) stable isotope ratios ($\delta^{13}C$, $\delta^{15}N$) and elemental concentrations, was characterized by Isotope Ratio Mass Spectrometry (IRMS)/Elemental Analyzer (EA) at LETIS (University of Liège, Belgium). The analysis was carried out at ~4 to 10 cm intervals using a VarioMicro Elementar analyser coupled to a precisION IRMS (LTe19-4). Prior to the analysis, the samples were acidified by exposing the freeze-dried and ground sediments to 37% HCl vapor for 10 hours to remove carbonates. Bulk N was considered to comprise primarily organic nitrogen given the generally low concentration of inorganic nitrogen in lake sediments. For LTe19-4, the analysis was additionally carried out on non-acidified samples to evaluate the influence of acidification on elemental concentrations and isotope ratios. The patterns of acidified and non-acidified samples were consistent for all four variables ($R^2$ > 0.94) indicating that the trends are reliable. All values used in this study for the three lakes are from acidified samples. Variations in carbon and nitrogen isotope ratios are expressed using the delta-notation, i.e., as differences (‰) relative to international standards (VPDB for carbon, AIR for nitrogen). Precision of the $\delta^{13}C$ and $\delta^{15}N$ measurements based on repeat analyses were ±0.27 and 0.97 SD, respectively. The carbon to nitrogen ratio (C/N) was calculated for each sample to estimate changes in the relative contribution of allochthonous and autochthonous organic matter (Meyers, 2003). C/N mass ratios were converted into atomic ratios by multiplying the values by 1.167.

### 3.2. Core chronology

The activities of $^{210}Pb$, $^{226}Ra$ and $^{232}Th$ were measured on 1 cm thick samples in cores

LLEs19-2, LTa19-3 and LTe19-4 with a low-background and high-efficiency well-type gamma detector (EPOC, University of Bordeaux, France) until negligible excess $^{210}$Pb was reached. The excess $^{210}$Pb activities ($^{210}Pb_{xs}$) were calculated by subtracting the measured $^{226}$Ra content from the total $^{210}$Pb content. The Constant Flux/Constant Sedimentation model (CF/CS, Appleby and Oldfield, 1978) was applied to the $^{210}Pb_{xs}$ to calculate a mean sediment accumulation rate, which was used to estimate an age for each sediment layer.

## 4. Results

### 4.1. Sedimentology

Figure 2 presents the SCOPIX image of the cores LLEs19-2 (Espinos), LTa19-3 (Tacámbaro) and LTe19-4 (Teremendo), along with the MS profiles and the abundance of clay (% < 2 μm) and fine silt (% 2-10 μm) fractions (Table S1).

[Insert Figure 2]

The sediment of LLEs19-2 was brownish dark (5YR 2/1, Munsell, 1975) with a fine organic-rich texture (average 24 % organic matter), dominated by silt (78±5%) and sand (20±5%) with a small proportion of clay (2.6±0.9%). Its MS profile ranged between 2.96 $10^{-4}$ and 6.30 $10^{-3}$ SI, with an average value of 1.55 $10^{-3}$ SI. The MS displayed a few positive excursions between 10 and 15 cm, 33 to 35 cm and 49-51 cm, underlying darker and coarser multi-millimeter laminations. The highest sand fraction (29%) corresponded to the darker laminations at 14-15 cm. In the upper part of the SCOPIX image, a vertical burrow disturbed several mm-scale laminations observed between 4 and 7 cm. The lower part of the core (from 35 to 53 cm) was marked by abundant gastropod shells, especially between 35 and 43 cm.

The background colour of sediment core LTa19-3 was dusky brown (5YR 2/2) with several darker (brownish black 5 YR 2/2) multi-millimeter laminations (Munsell, 1975). A

few shells were observed, especially in the lower core section (73-93.5 cm). The core was mainly composed of silt particles (80±7%) associated with 20±7% sand. The core section comprised between 39 and 52 cm was characterized by higher proportions of both clay (10 to 15%) and fine silt fractions (35 to 45%) than the core average (i.e. 5.5±3% and 26±8%, respectively). The LTa19-3 core displayed a similar range of MS variation from 3.48 $10^{-4}$ to 6.310$^{-3}$ SI as in the LLEs19-2 core but with a higher average value (2.03 $10^{-3}$ SI). The MS values were low (0.8 $10^{-3}$ SI) in the lower part of the core, increased up to 60 cm and then decreased irregularly from ~52 cm upwards. The organic matter content of the LTa19-3 core was on average 20% and reached up to 25% in the lower core section (60-93.5 cm).

The sediment in core LTe19-4 was brownish dark (5YR 2/1, Munsell, 1975) with a fine organic-rich texture (average 23% organic matter). The sediment was composed of silt (77±8%) and sand grains (23±8%) with a low proportion of clay particles (3.4±1%). The sediment texture comprised mm-scale darker laminations between 95 and 49 cm and was more homogeneous in the upper 49 cm. The MS profile of core LTe19-4 ranged from 2.37 $10^{-4}$ to 2.51 $10^{-3}$ SI. The MS displayed a minimum value between 103.5 and 100 cm, in an interval containing the highest sandy fraction of the core (45% at 100-101 cm). MS fluctuated between 93.5 and 49 with 4 distinct peaks, also visible in the SCOPIX image, at 93.5, 61, 54.5 and 49.5 cm, followed by a decline from 49 cm upwards.

### 4.2. Mineralogy

Andesite (i.e. plagioclase) and kaolinite were the two main minerals identified in the three studied sediment cores, associated with diopside (i.e. pyroxene), hornblende (i.e. amphibole) and/or forsterite (i.e. olivine) and quartz (Table S2). Carbonate minerals, ubiquitous in LLEs19-2 (except at 14-15 cm) and in LTe19-4, were represented by calcite, aragonite and/or dolomite. In contrast, carbonate minerals were absent from Tacámbaro. In addition, accessory minerals such as oxides (i.e. hematite, magnetite) or sulphide (pyrite) were detected in some

samples. The diffraction band observed between 20 and 30° 2θ revealed the presence of amorphous sedimentary components such as biogenic silica, organic matter or volcanic glass (e.g. Fagel et al., 2017).

In LLEs19-2 (Table S2a), andesite (plagioclase) was the most abundant mineral (43% ±12) followed by kaolinite (33% ±8). The secondary phases were pyroxene (i.e. diopside, 7% ±2.3) and carbonates, with both calcite (6.6% ±4.5) and aragonite (4.6% ±2.8). Quartz was present in trace amounts (1-3%) in all samples. Forsterite (2-6%) and hornblende (1-2%) were present in trace amounts. In addition to kaolinite, the phyllosilicates were also represented by traces of talc (≤ 1%), observed in a few samples.

With a core mean of 58% ±8, the relative abundance of kaolinite in LTa19-3 was higher than in LLEs19-2 with a range of variation between 37 and 76%. Traces of diaspore (0-2%) were suspected in the upper 60 cm core section whereas its abundance was slightly higher in the lower core section (3-6% - Table S2b). Andesite was the second most abundant mineral (24% ±5) in LTa19-3. Cristobalite represented an average abundance of 10%±3. Hornblende (< 3%) and diopside (< 1%) were present in low abundance in most samples. Quartz and hematite were ubiquitous whereas magnetite was identified in trace amounts (≤ 2%) in some samples. Traces of forsterite or talc were observed in only one sample. To get an overview of the mineral composition in LTa19-3 some XRD patterns are reported by core depth in Figure S1. With the exception of talc and hornblende, which were found in only one sample, most minerals were detected in all samples, but at variable intensities quantified by Topas. As an example, Figure S2 compares the raw XRD spectra of sample LTa19-3 15-16 cm with the Topas-derived reconstructed profile. For kaolinite, in particular, the unit cell parameters were modified from the structure given by Bish (1993b). A Rietveld refinement was first obtained by imposing two planes of preferential orientation (i.e. 001 and 100) and then by adjusting the

349 unit cell parameters (a, b, c, α, β and γ). The cif file obtained is reported in the supplementary
350 material (Text S1a).

351 Kaolinite (52% ±6) was the dominant mineral observed in LTe19-4, ranging from 41% at
352 54-55 cm to 65% at 100-101 cm. Kaolinite was followed by andesite (38% ±4). The other
353 magmatic minerals (i.e. diopside, forsterite and hornblende) were only observed in one or two
354 samples (Table S2c). Traces of cristobalite (< 2%) were only detected in the upper samples
355 (0-11 cm). Calcite (3.7% ±2) was present in low abundance in all samples, except in the
356 uppermost (0-1 cm). Quartz (2.7% ±0.7) was ubiquitous. Dolomite and hematite were
357 detected in traces in most samples.

358 In the three sediment~~ary~~ cores, kaolinite was the unique clay mineral evidenced by a large
359 reflection at 7.3Å in the bulk mineralogy of all samples (Figure S1), confirmed by SEM
360 observation (Figure S3). The TG curves displayed at least 2 main peaks between 50-130 °C
361 and 400-500 °C corresponding to 5-7% and 8-12% of mass loss, respectively (Figure 3). The
362 DTG curves specified the temperature of these endothermic reactions, i.e. 73-98 °C and 444-
363 474 °C respectively. A third exothermic peak was observed at 890-990°C associated with a
364 mass loss of ~3-5%. After heating up to 1200 °C the total weight loss averaged 20-33% of the
365 original sample weight.

366 [Insert Figure 3]

367 The FTIR analyses were done on two or three samples per core, those samples being
368 characterized by a range of abundance in kaolinite (i.e. 27 to 41% in LLEs19-2; 59 to 76% in
369 LTa19-3; 50 to 59% in LTe19-4). The samples from Tacámbaro and Teremendo displayed
370 similar FTIR spectra with two absorption bands in the 3690-3620 $cm^{-1}$ region and several
371 bands over 1000 and 500 $cm^{-1}$. Note the first two adsorption bands near 3700-3600 $cm^{-1}$ were

372 not detected in the two samples from LLEs19-2 that were characterized by the lowest
373 abundance of kaolinite in the bulk sediment.

374 [Insert Figure 4]

375 4.3. Sediment geochemistry

376 XRF element profiles, SCOPIX curves, clay abundance and organic geochemistry of the
377 three cores are plotted against core depth in Figure 5. For LLEs19-2, Ti covaried inversely
378 with the SCOPIX greyscale level (Figure 5) whereas Br mimicked the SCOPIX curve. The
379 darker sediment layers characterized by low SCOPIX levels corresponded to positive
380 incursions in Ti but negative incursions in Br. Sediment organic carbon (C) and nitrogen (N)
381 contents in LLEs19-2 followed a pattern similar to that of Br that may be associated with
382 organic matter in lake sediments (Ziegler et al., 2008; Davies et al., 2015). The relative
383 abundance of clay (< 2 µm fraction) followed a reverse pattern. Similarly, an opposite pattern
384 was observed for $\delta^{13}C$ that displayed the lowest (most $^{13}C$-depleted) values during periods of
385 elevated organic content and Br. C/N ratio and $\delta^{15}N$ in LLEs19-2 showed a gradual declining
386 trend towards the sediment surface and, overall, a relatively small range of variability.

387 [Insert Figure 5]

388 In LTa19-3, XRF elements and SCOPIX values showed similar coeval variation as in
389 LLEs19-2 (Figure 5). For example, a marked decrease in Ti counts observed between 58 and
390 62 cm corresponded to an increase in Br and SCOPIX values. Similarly, sediment C and N
391 covaried with Br, and decreasing $\delta^{13}C$ values were generally associated with increasing
392 organic content and Br. Clay (< 2 µm fraction) abundance showed little variability in the
393 lower part of the record (up to around 60 cm) whereon it followed a pattern somewhat similar
394 to Ti. C/N values showed a gradual decline in the lower part of the core (~90-65 cm), with a
395 distinct peak (> 25) at around 60 cm. Sediment $\delta^{15}N$ values showed few trends aside from a
396 step increase at around 60 cm.

For LTe19-4, Ti depicted an inverse trend with SCOPIX values and Br (Figure 5), consistent with LLEs19-2 and LTa19-3. Compared to the other two lakes, the variations in LTe19-4 were generally more stable aside from a pronounced decrease in Ti in the lower part of the core, between ~104 and 94 cm, and a corresponding increase in Br. Sediment C and N data are not available for this section of the core but both indicators reflect higher organic content between ~90 and 75 cm, consistent with slightly elevated Br. An increasing trend in C and N, and to a lesser extent in Br, was also observed in the upper 20 cm of the core. As in LLEs19-2, clay (< 2 µm fraction) abundance followed a pattern reverse to those observed in Br, C and N. Sediment $\delta^{13}C$ and C/N displayed distinctly low and high values, respectively, in the lower part of the core (i.e. ~75 cm downward), however, their variation was less clearly linked to variations in the XRF elements.

Regarding the RPCA, the first two PCs in core LLEs19-2 were sufficient to explain a cumulated variance of 74% (PC1 63%, PC2 11%). In the PC1-PC2 biplot diagram (Figure S4), the elements were clustered into two main groups aligned along the PC1 axis (see the correlation matrix given in Figure S4). Ti, Fe, Zr, Co, Sr and K (group 1) were aligned along the positive PC1 axis. Ni, Br and S associated with Si and Al (group 2) plotted along the negative PC1 axis. Ca varied along the positive PC2 axis. Pb and Mn were the less significant elements in the distribution, located in an intermediate position between PC1 and PC2.

In core LTa19-3, the elements were distributed in 3 groups and 69% of the variance was explained by 3 PCs (i.e. PC1 45%, PC2 14%, PC3 10%). The first two groups were aligned along the PC1 axis whereas group 3 was associated with the PC2 axis. Group 1 (Ti, Fe, Co, Zr, Mn and Pb but with a low contribution data in Figure S4) was associated with negative PC1 axis values whereas group 2 (S and Br associated with Ni and Al) was distributed along the positive PC1 axis. Group 3 (Ca, Sr and K) was clustered along the PC2 axis.

The RPCA analysis on LTe19-4 revealed 4 significant PCs (i.e. PC1 31%, PC2 21%, PC3 15%, PC4 13%) with a cumulative variance of 80%. The elements were scattered in the PC1-PC2 binary plot. At least 4 groups of elements were evidenced, i.e., Ni, Sr and Br (group 1), Co, Fe and Zr (group 2), Ti, Si and K (group 3) and, Pb and Ca (group 4) whereas Al and Sr were not significant (correlation matrix given in Figure S4).

### 4.4. Core chronology

In LLEs19-2, the $^{210}Pb_{xs}$ activity decreased from 288 mBq/g at 2.5 cm down to a negligible level at 16.5 cm, giving a low sediment accumulation rate of 0.09 cm/yr. For LTa19-3, the relatively constant $^{210}Pb_{xs}$ activity in the upper 5 cm suggested a mixed layer, which is consistent with the homogeneous texture underlined by the SCOPIX image (Figure 2). Below this mixed layer, the decrease in $^{210}Pb$ excesses resulted in a sediment accumulation rate of 0.6 cm/yr. LTe19-4 presented a rather regular exponential decrease of $^{210}Pbxs$ reaching negligible activities at about 25 cm, resulting in an intermediate sediment accumulation rate of 0.255 cm/yr compared to the other two lakes.

The age models of the three cores (Figure S5) were derived from the depth profiles of $^{210}Pb_{xs}$ in the upper 17, 23 and 61 cm of the sediment in cores LLEs19-2, LTe19-4 and LTa19-3, respectively. Assuming a surface age of AD2019 (i.e. coring year) and a constant sediment accumulation rate, LTa19-3 covers an interval of less than 160 yr whereas LLEs19-2 and LTE19-4 are well beyond the timescale of $^{210}Pb_{xs}$ with ~430 yr in LTe19-4 and $\leq$ 600 yr in LLEs19-2. In terms of temporal resolution, only the sedimentation rate for LTa19-3 would allow a sufficient resolution to investigate pluriannual ENSO variability with a sampling resolution of 1 cm (i.e. 1 cm corresponds to 1.7 years for LTa19-3, 4 years for LTe19-4 and 11 years for LLEs19-2).

## 5. Discussion

### 5.1. Origin of minerals

In the three studied crater lakes, the mineralogical assemblages are composed of variable proportions of primary minerals, probably derived from the volcanic crater substrate by erosion and runoff and secondary minerals formed by weathering and pedogenetic processes in the upper soil cover and possibly by hydrothermal alteration. The volcanic-derived primary minerals are dominated by andesite (up to 54% in LLEs19-2), which may be associated with some forsterite, diopside and/or amphibole (Table S2).

Concerning the clay minerals, the origin of kaolinite is most probably multifold. First, kaolinite is a ubiquitous secondary mineral, whose abundance reaches 65% in LTe19-4 and up to 74% in LTa19-3, whereas it accounts for less than 45% in LLEs19-2 (Table S2). SEM observations (Figure S3) confirmed that, at least, part of the kaolinite was formed by weathering of primary magmatic-derived plagioclase or Fe-Mg minerals. The presence of secondary kaolinite in the sediments of the three studied lakes probably reflects moderate hydrolysis conditions under tropical warm and humid conditions in the soils (e.g. Chamley, 1989) covering the internal crater flanks. Crater lakes represent small and closed sedimentary basins with a rapid source-to-sink transfer. Clay minerals in their sediments are useful indicators of paleoclimate conditions. However, pedogenesis is a slow process and the abundance of kaolinite observed in the crater lake sediments most likely reflects weathering conditions over the past millennia (Thiry, 2000).

Second, the broad reflection at 7.3 Å observed in the bulk XRD patterns of the Mexican lacustrine samples may indicate the presence of some halloysite-7 Å in addition to kaolinite. Halloysite-10 Å, renamed hydrohalloysite (Hatert et al., 2023), has been found in weathered or hydrothermally altered rocks, saprolites, and soils (Joussein et al., 2005). Hydrohalloysite is especially abundant in newly formed volcanic ash soils associated with quartz and

471 cristobalite, formed by hydrothermal alteration of volcanic rocks at low temperatures (e.g., in
472 New Zealand, Joussein et al., 2005). Such an origin is consistent with the volcanic substrate of
473 the lakes studied and the presence of cristobalite. Sample preparation may explain the absence
474 of hydrohalloysite in the crater lake samples, as hydrohalloysite can be quickly transformed
475 into halloysite-7 Å under ambient temperature and humidity conditions or by heating ≥ 40°C
476 (Joussein et al., 2005). In addition, hydrohalloysite has been considered as an early
477 weathering product in lateritic soils (Robert and Herbillon, 1990), representing an
478 intermediate weathering stage between recent soil rich in allophane and more weathered soils
479 rich in kaolinite and iron oxides in tropical and subtropical areas (Ndayiragije and Delvaux,
480 2004). The abundance of halloysite relative to kaolinite would decrease with increasing
481 weathering stage (Joussein et al., 2005).

482 In Tacámbaro, the association of kaolinite with some diaspore, confirmed by SEM
483 observation (Figure S3), indicates complete leaching of silica under strong hydrolysis
484 corresponding to an alitisation process. This process is indicative of stronger drainage that
485 may occur along the steepest slope of the crater flank. The presence of both kaolinite and
486 diaspore only in LTa19-3 emphasizes stronger chemical weathering conditions in the Lake
487 Tacámbaro catchment.

488 Among the other minerals observed, the presence of carbonates in all samples of
489 LLEs19-2, except in the dark layer at 14-15 cm (Figure 2), reflects a biological component
490 mainly associated with gastropod shells. In LTe19-4, some carbonates are detected by
491 XRD. These carbonates are probably authigenic and related to the productivity of the lake as
492 there are no carbonates in the watershed. Cristobalite is most probably related to the
493 presence of volcanic glass. In addition, the abundance of cristobalite, especially in LTa19-3 (≤
494 16%), could reflect the diatom productivity of the water column, as opal is an unstable
495 amorphous silica mineral. The transition from amorphous opal-A to crystallised opal-CT (CT

for cristobalite-tridymite) is a continuum controlled by a microscale dissolution-reprecipitation process in a near-surface environment (Jones and Renaut, 2007). Opal-A is progressively converted to opal-CT due to a decrease in d-spacing and porosity and an associated increase in density (Rice et al., 1995). Jones and Renaut (2007) emphasized that this process can be accelerated by the addition of Si from external sources. Indeed, such supply is supported in closed tropical crater lakes by silica-rich leachate solution delivered by monosialitisation and eventually alitisation processes.

5.2. Characterisation of 1:1 layer

In the bulk powder XRD patterns the broad reflection at 7.3 Å reflects the presence of a poorly ordered kaolinite, most probably in association with some halloysite-7 Å. Halloysite-7 Å is characterized by a broad reflection at 7.3 Å, which is difficult to decipher with a poorly ordered kaolinite, particularly when they are mixed (Brindley, 1980a). A few percentages of hydrohalloysite (cif file obtained reported on Text S1b) were found, in addition to kaolinite, in the bulk and clay < 2 μm fraction of at least one surface soil of the crater lake Teremendo (Figure S6). In the following text, the term kaolinite is used *sensu lato* for a mixture of kaolinite and some halloysite-7 Å.

The thermogram (TG) curves display two main mass losses characteristic of kaolinitic clays (Figure 4). The first endothermic mass loss at 40-130°C corresponds to the loss of adsorbed water. This pronounced endothermic reaction is consistent with the presence of both disordered kaolinite and halloysite-7 Å (Emmerich, 2010).

The second pronounced endothermic peak corresponds to the dehydroxylation of kaolinite/halloysite and its transformation in metakaolinite (e.g. Wang et al., 2011). The temperature of the reaction, as measured by DTG curves, is between 444 and 474°C, whereas the dehydroxylation of kaolinite often occurs at higher temperatures between 530 and 630°C

521 (Emmerich, 2010). However, the measured dehydroxylation temperature is influenced by
522 several factors, such as the mineral assemblage and, in particular, the abundance of kaolinite
523 in the sample (Anand and Gilkes, 1987), the crystallinity of kaolinite (Földvári, 2011) but also
524 the experimental conditions (Guggenheim and Van Groos, 2001; Heide and Földvari, 2006).
525 Anand and Gilkes (1987) observed an increase in dehydroxylation temperature from 454 to
526 491°C with increasing kaolinite abundance in soil samples. According to Földvári (2011), the
527 position of the dehydroxylation peak was observed in lower temperature ranges for disordered
528 kaolinites (530-570°C) than for ordered kaolinites (570-630°C). For the studied samples,
529 there is no clear relationship between the abundance of kaolinite in the bulk sample (i.e.
530 between 27 and 76%) and the dihydroxylation temperature. Therefore, the kaolinites studied
531 most probably correspond to extremely disordered crystals (Smykatz, 1974), associated with
532 some halloysite-7 Å.

533 A third mass loss of 3 to 5% occurring between 890 and 990°C corresponds to a small
534 exothermic peak associated with the crystallisation of mullite ($Al_2Si_2O_{13}$). Again, the
535 observed lower temperature range for this reaction (usually 940-1000°C) and the moderate
536 heat exchange confirm the disordered character of kaolinite (Emmerich, 2010) and the
537 presence of some halloysite-7 Å.

538 FTIR spectra (Figure 4) confirms the poorly crystallized character of kaolinite. Well-
539 ordered kaolinite is characterized by four absorption bands in the 3700-3600 $cm^{-1}$ range
540 associated with the stretching of OH-groups and by two absorption bands in the 1000-900 $cm^{-1}$
541 range associated with the bending (Bich et al., 2009). However, the FTIR spectra from
542 Tacámbaro and Teremendo samples display only two absorption bands between 3700 and
543 3620 $cm^{-1}$ (i.e. at 3689-3699 and 3618-3622 $cm^{-1}$ - Figure 4). The absence of vibration bands
544 at 3670 and 3650 $cm^{-1}$ indicates poorly order kaolinite (Vaculikova et al., 2011). It is also
545 supported by the presence of only one absorption band identified in the 1000-900 $cm^{-1}$ range

546 (i.e. between 908 and 916 $cm^{-1}$) due to the OH deformation of inner hydroxyl group
547 (Vaculikova et al., 2011). Note the peak near 540 $cm^{-1}$ that coincides with Al-O-Si
548 deformation in kaolinite (Madejová et al., 2010)

549 In addition to kaolinite, a mass loss (~5%) observed in the TG curve (Figure 3) between
550 the dehydratation and dehyhroxylation reactions reflects the presence of organic matter
551 (Mackenzie, 1957) and hydrated phases such as opal in the bulk sediment. In the FTIR spectra
552 (Figure 4), the absorption bands at 794-796 and 467-474 $cm^{-1}$ confirmed the presence of silica
553 minerals (i.e., quartz and cristobalite in XRD patterns). Related to the Si-O-Si bending
554 vibration, they usually grow from crystalline to non-crystalline varieties like opal A
555 (Graetsch, 1994). The absence of absorption bands between 3090 and 3460 $cm^{-1}$ confirms the
556 absence of gibbsite and boehmite (Kloprogge et al., 2002), which were not detected by XRD.
557 Note that the presence of diaspore, evidenced by SEM in LTa19-3 (Figure S3), was not
558 confirmed by FTIR (Frost et al., 1999).

559

560 5.3. Significance of kaolinite variability in the sedimentary record

561 Figure 5 shows the parallel evolution of kaolinite in regard to the Br/Ti ratio, i.e. a ratio
562 selected as a proxy for lake productivity (Agnihotri et al., 2008). The use of Br/Ti as a reliable
563 proxy for lake productivity in the studied lakes is supported by the bulk organic matter
564 geochemistry (Figure 5). In all three lakes, the concomitant increases in sediment organic
565 content (C and N) and Br/Ti were matched by generally low or declining $\delta^{13}C$ values, likely
566 related to increased phytoplankton productivity (Meyers, 2003). Similar low $\delta^{13}C$ values may
567 also be associated with terrestrial organic matter from C3 plants (typical values around
568 −27‰) (Meyers, 1997), however, the opposite patterns for detrital elements (such as Ti)
569 provide no evidence for increased catchment material fluxes. C/N values, often used to
570 indicate relative changes in autochthonous and allochthonous organic matter inputs, showed

few consistent changes but the generally low values point to a strong autochthonous component (Meyers, 2003) suggesting that the shifts in sediment C and N content (and thus Br/Ti) are tightly connected to primary production in the lake.

In LLEs19-2, the kaolinite abundance, which varies by a factor of 2 over the last 5 centuries follows a parallel trend with the Br/Ti ratio (Figure 6). The highest kaolinite abundance ~~of~~ (i.e. 45% at 23-24 cm) corresponds to a high Br/Ti ratio. The LLEs19-2 record displays four distinct intervals with higher kaolinite abundance: ca. 1450, 1600, 1760-1820 and 1940-1980 CE.

[Insert Figure 6]

In LTe19-4, the kaolinite abundance ranges from 41 to 65% over the last four centuries, with three intervals marked by higher kaolinite abundance at ~1640-1740, 1830-1900 and 1950-2019 CE. Although the range of variation is smaller than in LLEs19-2, the maximum abundance of kaolinite (i.e. 65% at 100-101 cm) also coincides with a pronounced positive excursion in the Br/Ti ratio around ca. 1650 CE. An increase in kaolinite is observed in the LLEs19-2 record within a similar time window (~1600 CE).

Due to a higher sedimentation rate, the core LTa19-3 covers only 160 years, allowing a high temporal resolution. In this short time period, the kaolinite profile (Figure 6) displays a broad variation (37-74%) with higher values observed in two intervals, i.e. in the lower part of the record (1865-1875 CE) and between 1930-1985 CE. As in core LLEs19-2, and to some extent in LTe19-4, the kaolinite abundance follows the evolution of the Br/Ti ratio in the lower part of the record (93-55 cm, ~1860-1925 CE). It is hypothesized that the covariance between kaolinite abundance and the Br/Ti ratios reflects lake productivity and, by extension, natural variations in lake level. In spring, warmer temperatures favour high biological productivity and keep lake level low through evaporation. The onset of rainfall brings nutrients and detrital material, including kaolinite-rich clayey particles, into the lake. The

sedimentation of kaolinite may then be related to its rapid adsorption on the abundant organic matter present in the water column (Guo et al., 2023) and to the settling of the organo-mineral aggregates due to their density. This is supported by the low abundance of clay-sized particles during organic-rich periods, particularly distinct in LLEs19-2 (Figure 5).

There is no obvious relationship between the regional (Harris et al., 2020) or local temperature data (CONAGUA-SMN web platform, http://clicom-mex.cicese.mx) and the kaolinite profile in core LTa19-3. The lowest temperature interval recorded in the local meteorological data (1950-1990 CE) does not coincide with the lowest kaolinite abundance in LTa19-3. The sharp increase in kaolinite observed during 1925-1930 CE occurs during an interval of low regional temperatures but it is consistent with an increase in local precipitation.

In the upper section of core LTa19-3, there is no clear relationship between the Br/Ti ratio and kaolinite (Figure 6). The kaolinite abundance varies rather in parallel with Ti, although the different resolution of the two proxies prevents a detailed comparison. This sharp change probably reflects a local disturbance around Lake Tacámbaro. Ortega-Guerrero et al. (2021) reported that the water level of Lake Tacámbaro was regulated by the construction of an artificial canal in the early 20$^{th}$ century. The exact date of this human intervention is unknown. The distinct peak in C/N values at around 60 cm (Figure 5), coincident with the decoupling between kaolinite and Br/Ti ratio (Figure 6), may well indicate a transient increase in catchment inputs associated with the construction work. After the construction of the canal, the sharp increase in kaolinite occurs during an interval of increased local rainfall. This change in local meteorological conditions (i.e. the sharpest change during the 20$^{th}$ century) probably enhances surface runoff, delivering more detrital elements and kaolinite to Lake Tacámbaro.

## Conclusions

- Disordered kaolinite is the dominant secondary mineral present in all sediment samples from the 3 crater lakes investigated. This clay mineral is partly formed by moderate hydrolysis, a process consistent with the regional tropical warm and humid conditions of Central Mexico.
- The broad reflection at 7.3 Å observed in the bulk XRD patterns of the Mexican lacustrine samples underlines the presence of some halloysite-7 Å in addition to kaolinite. Halloysite is most probably formed by hydrothermal alteration of volcanic glasses.
- The presence of diaspore in Lake Tacámbaro probably reflects a more efficient local drainage along the steepest slope of the crater, resulting in complete removal of silica.
- Statistical treatment of the XRF core scanner data indicates an opposite relationship between detrital elements (Ti, K, Fe) and organic matter-related elements (Br, S, Ni).
- In lakes Los Espinos and Teremendo, the kaolinite abundance is the highest when the detrital flux (e.g. Ti) is the lowest and the organic matter flux is the highest. Kaolinite may be adsorbed onto the organic matter particles present in the water column and then settle to the lake bottom. Under natural conditions, the kaolinite abundance in the crater lake sediments may be a proxy for lake productivity and an indirect proxy for lake level (i.e. higher kaolinite abundance associated with lower lake level).
- For Lake Tacámbaro, the construction of a canal in the early 20$^{th}$ century to regulate the lake level suppresses the link between the kaolinite and lake productivity observed in the lower core section (pre-1925 CE). In the upper core section (i.e. post 1925 CE), kaolinite covaries with detrital elements such as Ti which are carried by surface runoff. The abundance of kaolinite is sensitive to rainfall intensity particularly when human intervention regulates lake levels.

## Acknowledgments

The fieldwork was done in June 2019 by N. Fagel and I. Israde-Alcantara, with the help of Luis Matilde Gacia, Julio Cañas, David Sanchez and Angel Zamudio. Thanks to Arturo Chacon for providing a boat location. Part of the analysis costs was supported by a FNRS funding for the PDR proposal HolMecl 2020-2025. The authors thank Joel Otten and Nicolas Delmelle (Geology, ULiège) for their technical support with the sedimentological and mineralogical preparations and analyses. Subsampling and sedimentological analyses were done as part of the master thesis of Gaelle Wanlin. Prof. Frédéric Boulvain (Sedimentology, ULiège) brought his expertise on sedimentological features and core description. Prof. Frédéric Hatert (Mineralogy, ULiège) helped with the TOPAS software. SEM-EDS observations were made with the support of Régis Parvaud, ARCEN analytical platform of the University of Burgundy (Dijon, France).

## References


Adrian, R., O'Reilly, C.M., Zagarese, H., Baines, S.B., Hessen, D.O., Keller, W., Livingstone, D.M., Sommaruga, R., Straile, D., Van Donk, E., 2009. Lakes as sentinels of climate change. Limnology and oceanography 54, 2283-2297.

Agnihotri, R., Altabet, M.A., Herbert, T.D., Tierney, J.E., 2008. Subdecadally resolved paleoceanography of the Peru margin during the last two millennia. Geochemistry, Geophysics, Geosystems 9.

Alcocer, J., Escobar, E., Lugo, A., 2000. Water use (and abuse) and its effects on the crater-lakes of Valle de Santiago, Mexico. Lakes & Reservoirs: Research & Management 5, 145-149.

Anand, R., Gilkes, R., 1987. An application of thermogravimetry to quantitative studies of feldspar alteration in soils. Journal of Thermal Analysis and Calorimetry 32, 1163-1175.

Appleby, P.G., Oldfield, F., 1978. The calculation of lead-210 dates assuming a constant rate of supply of unsupported 210Pb to the sediment. Catena 5, 1-8.

Barron, J.A., Metcalfe, S.E., Addison, J.A., 2012. Response of the North American monsoon to regional changes in ocean surface temperature. Paleoceanography 27.

Bartington-Instruments, 2008. OM0408 - Operation manual for MS2 magnetic susceptibility system. Bartington Instruments Limited. Oxford, England.

Bich, C., Ambroise, J., Péra, J., 2009. Influence of degree of dehydroxylation on the pozzolanic activity of metakaolin. Applied Clay Science 44, 194-200.

Bish, D.L., 1993a. Rietveld refinement of the kaolinite structure at 1.5 K. Clays and Clay Minerals 41, 738-744.

Bish, D.L., 1993b. Studies of clays and clay minerals using X-ray powder diffraction and the Rietveld method. Los Alamos National Lab., NM (United States).

Bradbury, J.P., 2000. Limnologic history of Lago de Patzcuaro, Michoacan, Mexico for the past 48,000 years: impacts of climate and man. Palaeogeography, Palaeoclimatology, Palaeoecology 163, 69-95.

Briddon, C.L., Metcalfe, S., Taylor, D., Bannister, W., Cunanan, M., Santos-Borja, A.C., Papa, R.D., McGowan, S., 2023. Changing water quality and thermocline depth along an aquaculture gradient in six tropical crater lakes. Hydrobiologia 850, 283-299.

Brindley, G.W., 1980a. Order-disorder in the clay mineral structures, in: Brindley, G.W., Brown, G. (Eds.), Crystal Structures of Clay Minerals and their X-ray Identification. Mineralogical Society, London, pp. 125-196.

Brindley, G.W., 1980b. Quantative analysis of clay mixtures, in: Brindley, G.W., Brown, G. (Eds.), Crystal Structures of Clay Minerals and their X-ray Identification. Mineralogical Society, London, pp. 125-196.

Caballero, M., Vázquez, G., Ortega, B., Favila, M.E., Lozano-García, S., 2016. Responses to a warming trend and "El Niño" events in a tropical lake in western México. Aquatic Sciences 78, 591-604.

Candès, E.J., Li, X., Ma, Y., Wright, J., 2011. Robust principal component analysis? Journal of Association for computing machinery 57, 1-37.

Castro, C.L., McKee, T.B., Pielke, R.A., 2001. The relationship of the North American monsoon to tropical and North Pacific sea surface temperatures as revealed by observational analyses. Journal of Climate 14, 4449-4473.

Chamley, H., 1989. Clay formation through weathering. Clay sedimentology, 21-50.

Cifuentes, R.M.U., Fucugauchi, J.U., 1999. Paleomagnetic study of the Valle de Santiago volcanics, Michoacán-Guanajuato volcanic field, Mexico. Geofísica Internacional 38, 217-230.

Cobb, K.M., Westphal, N., Sayani, H.R., Watson, J.T., Di Lorenzo, E., Cheng, H., Edwards, R., Charles, C.D., 2013. Highly variable El Niño–southern oscillation throughout the Holocene. Science 339, 67-70.

Davies, S.J., Lamb, H.F., Roberts, S.J., 2015. Micro-XRF core scanning in palaeolimnology: recent developments. Micro-XRF studies of sediment cores: Applications of a non-destructive tool for the environmental sciences, 189-226.

Davis, J.C., 2002. Statistics and data analysis in Geology. Wiley & sons, New York.

Douglas, M.W., Maddox, R.A., Howard, K., Reyes, S., 1993. The mexican monsoon. Journal of Climate 6, 1665-1677.

Drits, V., Besson, G., Muller, F., 1995. An improved model for structural transformations of heat-treated aluminous dioctahedral 2: 1 layer silicates. Clays and Clay minerals 43, 718-731.

Emmerich, K., 2010. Thermal analysis in the characterization and processing of industrial minerals.

Fagel, N., Alvarez, D., Namur, O., Devidal, J.-L., Nuttin, L., Schmidt, S., Jana, P., Torrejon, F., Bertrand, S., Araneda, A., 2017. Lacustrine record of last millennia eruptions in Northern Chilean Patagonia (45–47° S). The Holocene 27, 1227-1251.

Ferrari, L., Orozco-Esquivel, T., Manea, V., Manea, M., 2012. The dynamic history of the Trans-Mexican Volcanic Belt and the Mexico subduction zone. Tectonophysics 522, 122-149.

Filzmoser, P., Fritz, H., Kalcher, K., 2018. pcaPP: Robust PCA by Projection Pursuit. R Foundation for Statistical Computing, Vienna, Austria.

718 Földvári, M., 2011. Handbook of thermogravimetric system of minerals and its use in geological practice.
719 Geological Institute of Hungary Budapest.
720 Frost, R.L., Kloprogge, J.T., Russell, S.C., Szetu, J., 1999. Dehydroxylation and the vibrational spectroscopy of
721 aluminum (oxo) hydroxides using infrared emission spectroscopy. Part III: diaspore. Applied
722 Spectroscopy 53, 829-835.
723 Frugone-Álvarez, M., Latorre, C., Giralt, S., Polanco-Martínez, J., Bernárdez, P., Oliva-Urcia, B., Maldonado,
724 A., Carrevedo, M.L., Moreno, A., Delgado Huertas, A., 2017. A 7000-year high-resolution lake
725 sediment record from coastal central Chile (Lago Vichuquén, 34° S): implications for past sea level and
726 environmental variability. Journal of Quaternary Science 32, 830-844.
727 Garrett, R.G., Garrett, M.R.G., 2018. Package 'rgr'. Appl Geochemistry EDA.
728 Gomez-Tagle Chavez, A., Bernal-Brooks, F., Alcocer, J., 2002. Sensitivity of Mexican water bodies to regional
729 climatic change: three study alternatives applied to remote sensed data of Lake Patzcuaro.
730 Hydrobiologia 467, 169-176.
731 Graetsch, H., 1994. Structural characteristics of opaline and microcrystalline silica minerals. Reviews in
732 Mineralogy and Geochemistry 29, 209-232.
733 Guggenheim, S., Van Groos, A.K., 2001. Baseline studies of the clay minerals society source clays: thermal
734 analysis. Clays and Clay Minerals 49, 433-443.
735 Guilbaud, M.-N., Siebe, C., Layer, P., Salinas, S., 2012. Reconstruction of the volcanic history of the
736 Tacámbaro-Puruarán area (Michoacán, México) reveals high frequency of Holocene monogenetic
737 eruptions. Bulletin of volcanology 74, 1187-1211.
738 Guo, C., Guo, L., Bass, S., Manning, A.J., Jin, Z., Zhou, Y., 2023. On the role of organic matter composition in
739 fresh-water kaolinite flocculation. Journal of Environmental Management 345, 118576.
740 Harris, I., Osborn, T.J., Jones, P., Lister, D., 2020. Version 4 of the CRU TS monthly high-resolution gridded
741 multivariate climate dataset. Scientific data 7, 109.
742 Hasenaka, T., Carmichael, I.S.E., 1985. The cinder cones of Michoacan-Guanajuato, central Mexico: their age,
743 volume and distribution, and magma discharge rate. Journal of Volcanology and Geothermal Research
744 25, 105-124.
745 Hatert, F., Mills, S.J., Pasero, M., Miyawaki, R., Bosi, F., 2023. CNMNC guidelines for the nomenclature of
746 polymorphs and polysomes. Mineralogical Magazine 87, 225-232.

747 Heide, K., Földvari, M., 2006. High temperature mass spectrometric gas-release studies of kaolinite Al2 [Si2O5
748 (OH) 4] decomposition. Thermochimica Acta 446, 106-112.
749 Hemminger, W.F., Cammenga, H.K., 1989. Methoden des thermischen analyse. Springer Verlag, Heidelberg,
750 Germany.
751 Hernández-Morales, R., 2011. Fitoplancton de los lagos cráter de Michoacán, México.
752 Hernández-Morales, R., Ortega, M., Sánchez, J., Alvarado, R., Aguilera, M., 2011. Distribución estacional del
753 fitoplancton en un lago cálido monomíctico en Michoacán, México. Biológicas Revista de la DES
754 Ciencias Biológico Agropecuarias Universidad Michoacana de San Nicolás de Hidalgo 13, 21-28.
755 Higgins, R.W., Chen, Y., Douglas, A.V., 1999. Interannual variability of the North American warm season
756 precipitation regime. Journal of Climate 12, 653-680.
757 Holmes, J.A., Metcalfe, S.E., Jones, H.L., Marshall, J.D., 2016. Climatic variability over the last 30 000 years
758 recorded in La Piscina de Yuriria, a Central Mexican crater lake. Journal of Quaternary science 31, 310-
759 324.
760 Jones, B., Renaut, R.W., 2007. Microstructural changes accompanying the opal-A to opal-CT transition: New
761 evidence from the siliceous sinters of Geysir, Haukadalur, Iceland. Sedimentology 54, 921-948.
762 Joussein, E., Petit, S., Churchman, J., Theng, B., Righi, D., Delvaux, B., 2005. Halloysite clay minerals—a
763 review. Clay minerals 40, 383-426.
764 Kienel, U., Bowen, S.W., Byrne, R., Park, J., Böhnel, H., Dulski, P., Luhr, J.F., Siebert, L., Haug, G.H.,
765 Negendank, J.F., 2009. First lacustrine varve chronologies from Mexico: impact of droughts, ENSO and
766 human activity since AD 1840 as recorded in maar sediments from Valle de Santiago. Journal of
767 Paleolimnology 42, 587-609.
768 Kloprogge, J.T., Ruan, H.D., Frost, R.L., 2002. Thermal decomposition of bauxite minerals: infrared emission
769 spectroscopy of gibbsite, boehmite and diaspore. Journal of materials science 37, 1121-1129.
770 Lind, O.T., Doyle, R., Vodopich, D.S., Trotter, B.G., Limón, J.G., Dcivalos-Lind, L., 1992. Clay turbidity:
771 Regulation of phytoplankton production in a large, nutrient-rich tropical lake. Limnology and
772 Oceanography 37, 549-565.
773 Lorentz, B., Shanahan, N., Stetsko, Y.P., Zayed, A., 2018. Characterization of Florida kaolin clays using
774 multiple-technique approach. Applied Clay Science 161, 326-333.
775 Mackenzie, R.C., 1957. The differential thermal investigation of clays.

776 Madejová, J., Balan, E., Petit, S., 2010. Application of vibrational spectroscopy to the characterization of
777 phyllosilicates and other industrial minerals.
778 McPhaden, M.J., Zebiak, S.E., Glantz, M.H., 2006. ENSO as an integrating concept in earth science. science
779 314, 1740-1745.
780 Meyers, P.A., 1997. Organic geochemical proxies of paleoceanographic, paleolimnologic, and paleoclimatic
781 processes. Organic geochemistry 27, 213-250.
782 Meyers, P.A., 2003. Applications of organic geochemistry to paleolimnological reconstructions: a summary of
783 examples from the Laurentian Great Lakes. Organic geochemistry 34, 261-289.
784 Migeon, S., Weber, O., Faugeres, J.-C., Saint-Paul, J., 1998. SCOPIX: a new X-ray imaging system for core
785 analysis. Geo-Marine Letters 18, 251-255.
786 Moore, D.M., Reynolds, R.C., 1989. X-ray Diffraction and the Identification and Analysis of Clay Minerals.
787 Oxford university press Oxford.
788 Morales, R.H., Murillo, M.O., Villanueva, R.A., Heredia, J.S., Zarco, F.M., 2008. Variación anual del
789 fitoplancton en el lago cráter La Alberca de Tacámbaro, Michoacán, México. Biológicas Revista de la
790 DES Ciencias Biológico Agropecuarias Universidad Michoacana de San Nicolás de Hidalgo 10, 5-17.
791 Munsell, C., 1975. Munsell soil color charts: Munsell Color. Baltimore, Maryland.
792 Ndayiragije, S., Delvaux, B., 2004. Selective sorption of potassium in a weathering sequence of volcanic ash
793 soils from Guadeloupe, French West Indies. Catena 56, 185-198.
794 Ortega-Guerrero, B., Caballero, M., Israde-AlcáNtara, I., 2021. The Holocene record of Alberca de Tacámbaro,
795 a tropical lake in western Mexico: evidence of orbital and millennial-scale climatic variability. Journal
796 of Quaternary Science 36, 649-663.
797 Park, J., Byrne, R., Böhnel, H., 2019. Late Holocene climate change in Central Mexico and the decline of
798 Teotihuacan. Annals of the American Association of Geographers 109, 104-120.
799 Patterson, E., Swaffield, R., 1987. Thermal analysis, in: M.J., W. (Ed.), Handbook of determinative methods in
800 clay mineralogy. Blackie and Son Limited, Glasgow, UK, pp. 99-132.
801 Pedro, G., 1968. Distribution des principaux types d'altération chimique à la surface du globe. Présentation d'une
802 esquisse géographique. Rev. Géogr. Phys. Géol. Dyn 2, 5.
803 R Development Core Team, R., 2013. R: A language and environment for statistical computing.

804 Rice, S., Freund, H., Huang, W., Clouse, J., Isaacs, C., 1995. Application of Fourier transform infrared
805 spectroscopy to silica diagenesis; the opal-A to opal-CT transformation. Journal of Sedimentary
806 Research 65, 639-647.
807 Rietveld, H., 1967. Line profiles of neutron powder-diffraction peaks for structure refinement. Acta
808 Crystallographica 22, 151-152.
809 Robert, M., Herbillon, A., 1990. Application aux argiles de sols. Genèse, nature et rôle des constituants argileux
810 dans les principaux types de sols des environnements volcaniques insulaires, Matériaux argileux.
811 Structure, propriétés et applications, pp. 539-576.
812 Saalfeld, H., Wedde, M., 1974. Refinement of the crystal structure of gibbsite, A1 (OH) 3. Zeitschrift für
813 Kristallographie-Crystalline Materials 139, 129-135.
814 Siebe, C., Guilbaud, M., Salinas, S., Chedeville-Monzo, C., 2012. Eruption of Alberca de los Espinos tuff cone
815 causes transgression of Zacapu lake ca. 25,000 yr BP in Michoacán, México, IAS 4IMC Conference,
816 Auckland, New Zeland, pp. 74-75.
817 Sigala, I., Caballero, M., Correa-Metrio, A., Lozano-García, S., Vázquez, G., Pérez, L., Zawisza, E., 2017. Basic
818 limnology of 30 continental waterbodies of the Transmexican Volcanic Belt across climatic and
819 environmental gradients. Boletín de la Sociedad Geológica Mexicana 69, 313-370.
820 Singer, A., 1984. The paleoclimatic interpretation of clay minerals in sediments—a review. Earth-Science
821 Reviews 21, 251-293.
822 Smykatz, K., 1974. The determination of the degree of (dis-) order of kaolinites by means of differential thermal
823 analysis.
824 Soria-Caballero, D.C., Garduño-Monroy, V.H., Alcalá, M., Velázquez-Bucio, M.M., Grassi, L., 2019. Evidence
825 for quaternary seismic activity of the La Alberca-Teremendo fault, Morelia region, Trans-Mexican
826 Volcanic Belt. Revista Mexicana de Ciencias Geológicas 36, 242-258.
827 Środoń, J., 2002. Quantitative mineralogy of sedimentary rocks with emphasis on clays and with applications to
828 K-Ar dating. Mineralogical Magazine 66, 677-687.
829 Thiry, M., 2000. Palaeoclimatic interpretation of clay minerals in marine deposits: an outlook from the
830 continental origin. Earth-Science Reviews 49, 201-221.
831 Vaculikova, L., Plevova, E., Vallova, S., Koutnik, I., 2011. Characterization and differentiation of kaolinites
832 from selected Czech deposits using infrared spectroscopy and differential thermal analysis.

833 Wang, H., Li, C., Peng, Z., Zhang, S., 2011. Characterization and thermal behavior of kaolin. Journal of Thermal
834 Analysis and Calorimetry 105, 157-160.
835 Warr, L.N., 2022. Earth's clay mineral inventory and its climate interaction: A quantitative assessment. Earth-
836 Science Reviews, 104198.
837 Weaver, C.E., 1989. Clays, muds, and shales. Elsevier.
838 Winder, M., Reuter, J.E., Schladow, S.G., 2009. Lake warming favours small-sized planktonic diatom species.
839 Proceedings of the Royal Society B: Biological Sciences 276, 427-435.
840 Wogau, K.H., Arz, H.W., Böhnel, H.N., Nowaczyk, N.R., Park, J., 2019. High resolution paleoclimate and
841 paleoenvironmental reconstruction in the Northern Mesoamerican Frontier for Prehistory to Historical
842 times. Quaternary Science Reviews 226, 106001.
843 Żarczyński, M., Wacnik, A., Tylmann, W., 2019. Tracing lake mixing and oxygenation regime using the Fe/Mn
844 ratio in varved sediments: 2000 year-long record of human-induced changes from Lake Żabińskie (NE
845 Poland). Science of the Total Environment 657, 585-596.
846 Ziegler, M., Jilbert, T., de Lange, G.J., Lourens, L.J., Reichart, G.J., 2008. Bromine counts from XRF scanning
847 as an estimate of the marine organic carbon content of sediment cores. Geochemistry, Geophysics,
848 Geosystems 9.

849

850 **List of figures**

851 Figure 1. (A) Regional map of North America with the location of the studied area (white
852 square), i.e. the Trans-Mexican Volcanic Belt (TMVB) in Central Mexico, and the boreal
853 summer position of the Inter-tropical Convergence Zone (ITCZ). (B) Enlarged map
854 showing the location of the three studied crater lakes Los Espinos (LLEs), Tacámbaro
855 (LTa) and Teremendo (LTe). (C) Photos of the three crater lakes (Google Earth image,
856 2022). (D) Climatographs of the meteorological stations located nearby the three crater
857 lakes showing the monthly average temperature and precipitation data from 1981 to 2010
858 (Source: Servicio Meteorológico Nacional, Mexico, http://smn.cna.gob.mx/).
859 Figure 2. Lithology of cores LLEs19-2, LTa19-3 and LTe19-4. SCOPIX high-resolution
860 image of the core, magnetic susceptibility profiles (plain black line) and abundance of clay

(% < 2 μm - upper axis, grey plain line) and fine silt (% 2-10 μm - lower axis, black dashed line) fraction. Grain-size data are reported in Table SM1.

Figure 3. STA curves of sample LTa19-3 88-89 cm that contains the highest abundance of kaolinite in the analyzed bulk sediments. TG, loss of weight (%): black curve, DSC: green curve, DTG: blue curve.

Figure 4. Examples of FTIR curves on a selection of kaolinite-rich samples.

Figure 5. Selection of clr transformed XRF element profiles ($Ti_{clr}$, $Br_{clr}$) and elemental ratio (Br/Ti) reported together with SCOPIX, PC1 score data, organic geochemistry (carbon [C] and nitrogen [N] concentrations and isotope ratios), and relative clay abundance (<2 μm fraction). Note the scale for SCOPIX values and clay abundance is inverted to present a parallel evolution of the profiles.

Figure 6. Temporal evolution of relative kaolinite abundance, Ti and Br/Ti in the studied three sediment cores over the past centuries. Note that the age estimates, based on $^{210}Pb_{xs}$ data, are tentative beyond the past century. Comparison between temporal evolution of relative kaolinite abundance, Ti and Br/Ti in core LTa19-3 and regional and local temperature and precipitation trends over the past decades. Regional climate trends (indicated in colour) are based on the CRU TS (Climatic Research Unit gridded Time Series) dataset (CRU TS Version 4.06 - Harris et al., 2020) and local (indicated in grey) climate data derive from a nearby weather station (station Tacámbaro, 16123) accessed through the CONAGUA-SMN web platform (http://clicom-mex.cicese.mx). The annual mean for precipitation is 1168 mm/yr for Tacámbaro, 896 mm/yr for Villa Jimenez station (nearby lake Los Espinos) and 700 mm/yr for Teremendo. Thickened lines depict lowess smooth curves (span 0.1). The presumed timing of the canal construction is indicated with a grey vertical bar.

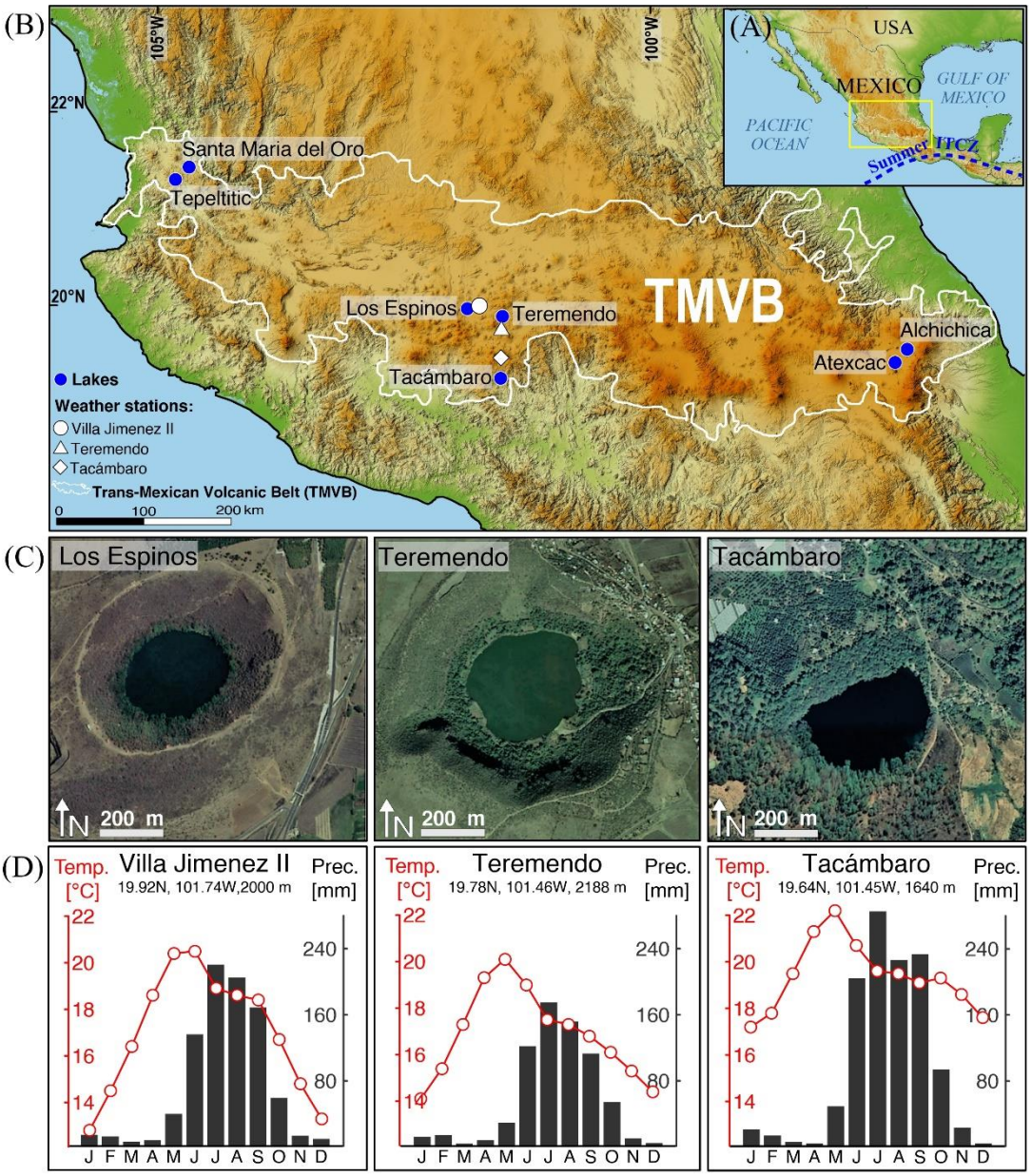


885

886 **Figure 1**

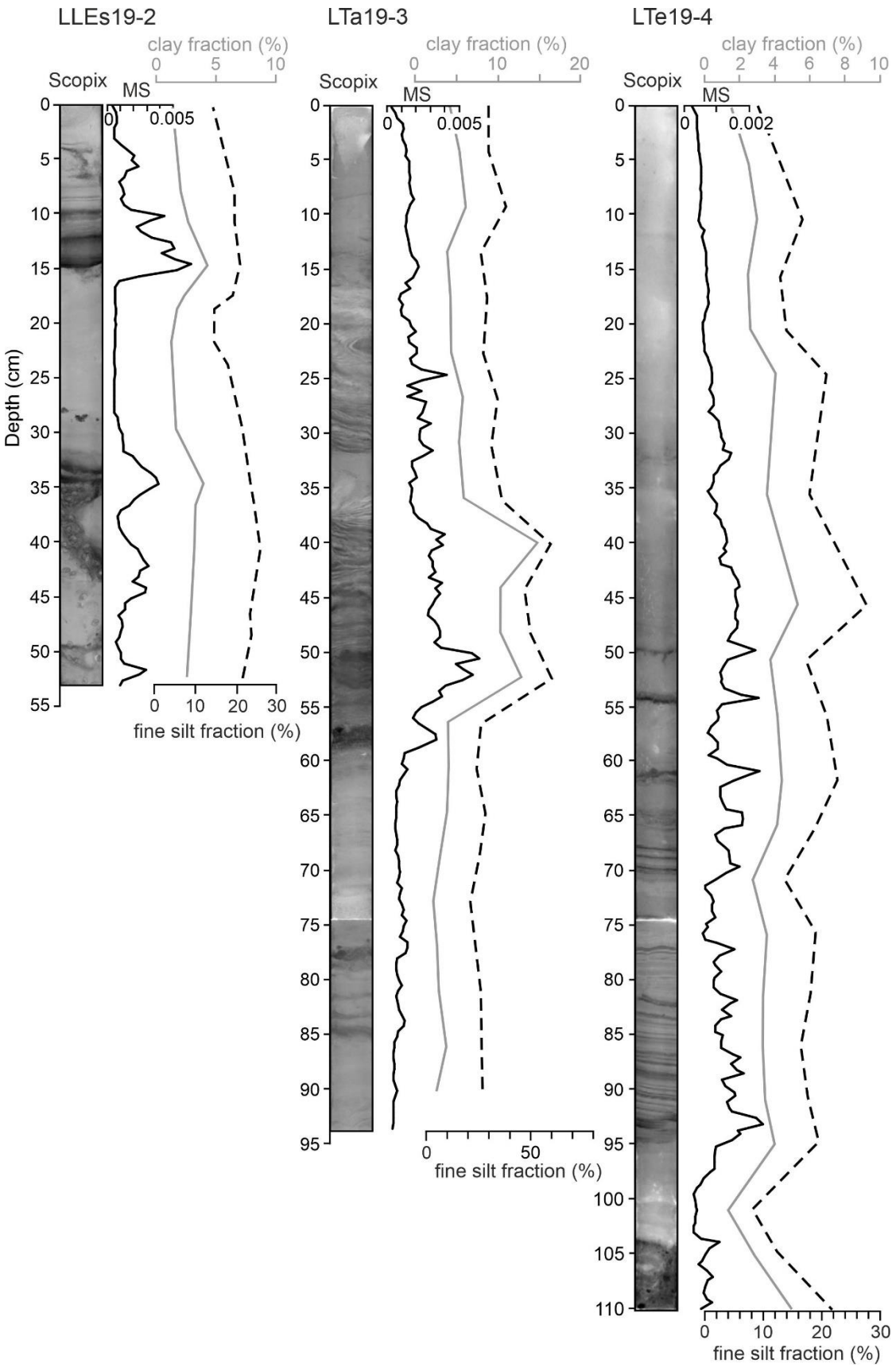


887

888 **Figure 2**

889

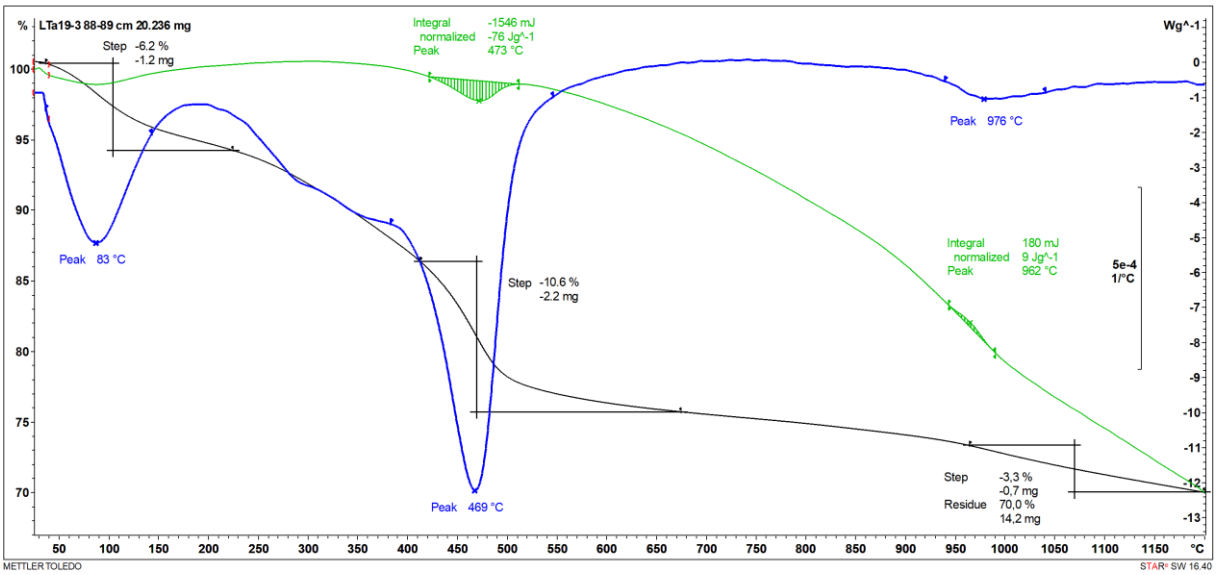
% LTa19-3 88-89 cm 20.236 mg
Step -6.2 %
-1.2 mg
Integral -1546 mJ
normalized -76 Jg^-1
Peak 473 °C
Wg^-1
Peak 976 °C
Peak 83 °C
Step -10.6 %
-2.2 mg
Integral 180 mJ
normalized 9 Jg^-1
Peak 962 °C
5e-4
1/°C
Peak 469 °C
Step -3,3 %
-0,7 mg
Residue 70,0 %
14,2 mg
°C
METTLER TOLEDO
STAR° SW 16.40

**Figure 3**

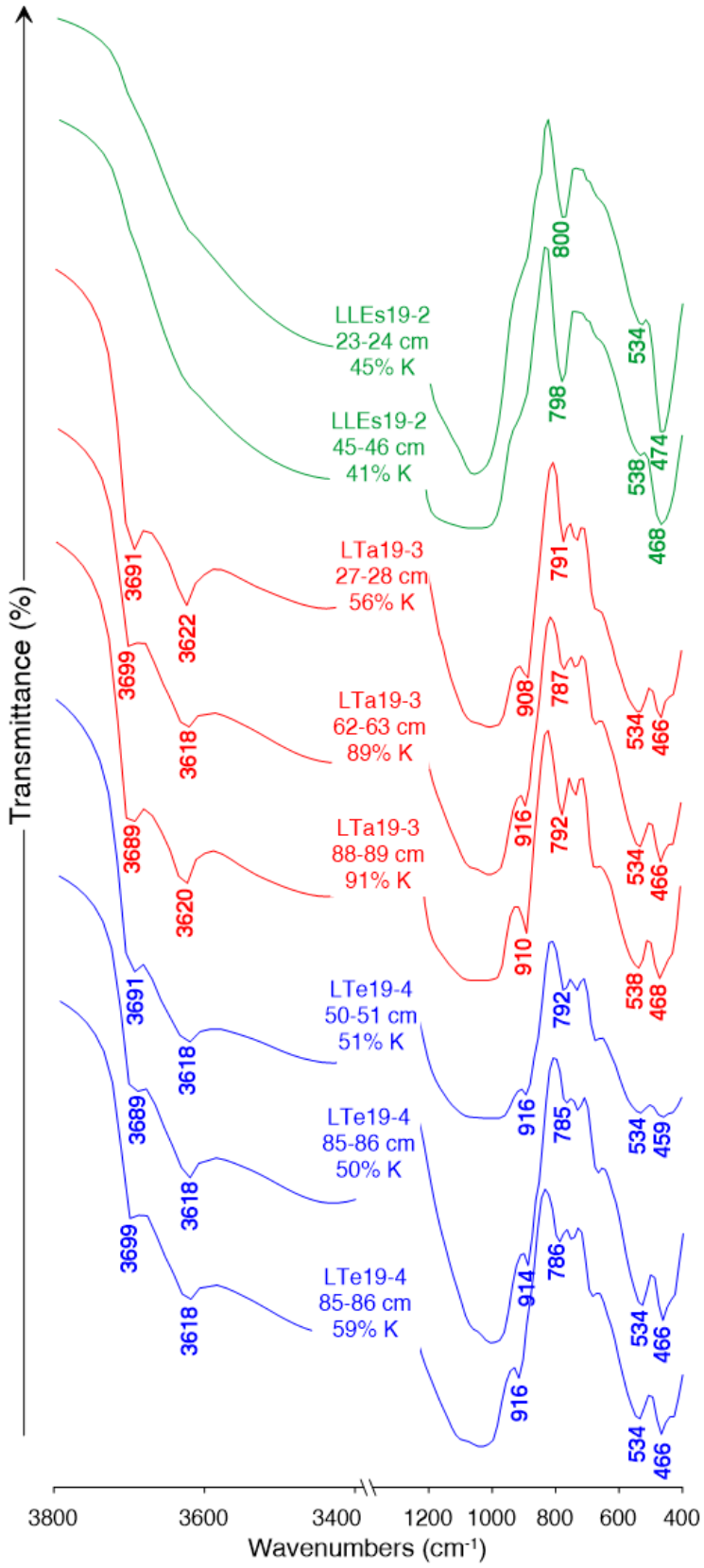
Transmittance (%)
LLEs19-2
23-24 cm
45% K
LLEs19-2
45-46 cm
41% K
LTa19-3
27-28 cm
56% K
LTa19-3
62-63 cm
89% K
LTa19-3
88-89 cm
91% K
LTe19-4
50-51 cm
51% K
LTe19-4
85-86 cm
50% K
LTe19-4
85-86 cm
59% K
3800
3600
3400
1200
1000
800
600
400
Wavenumbers (cm-1)

**Figure 4**

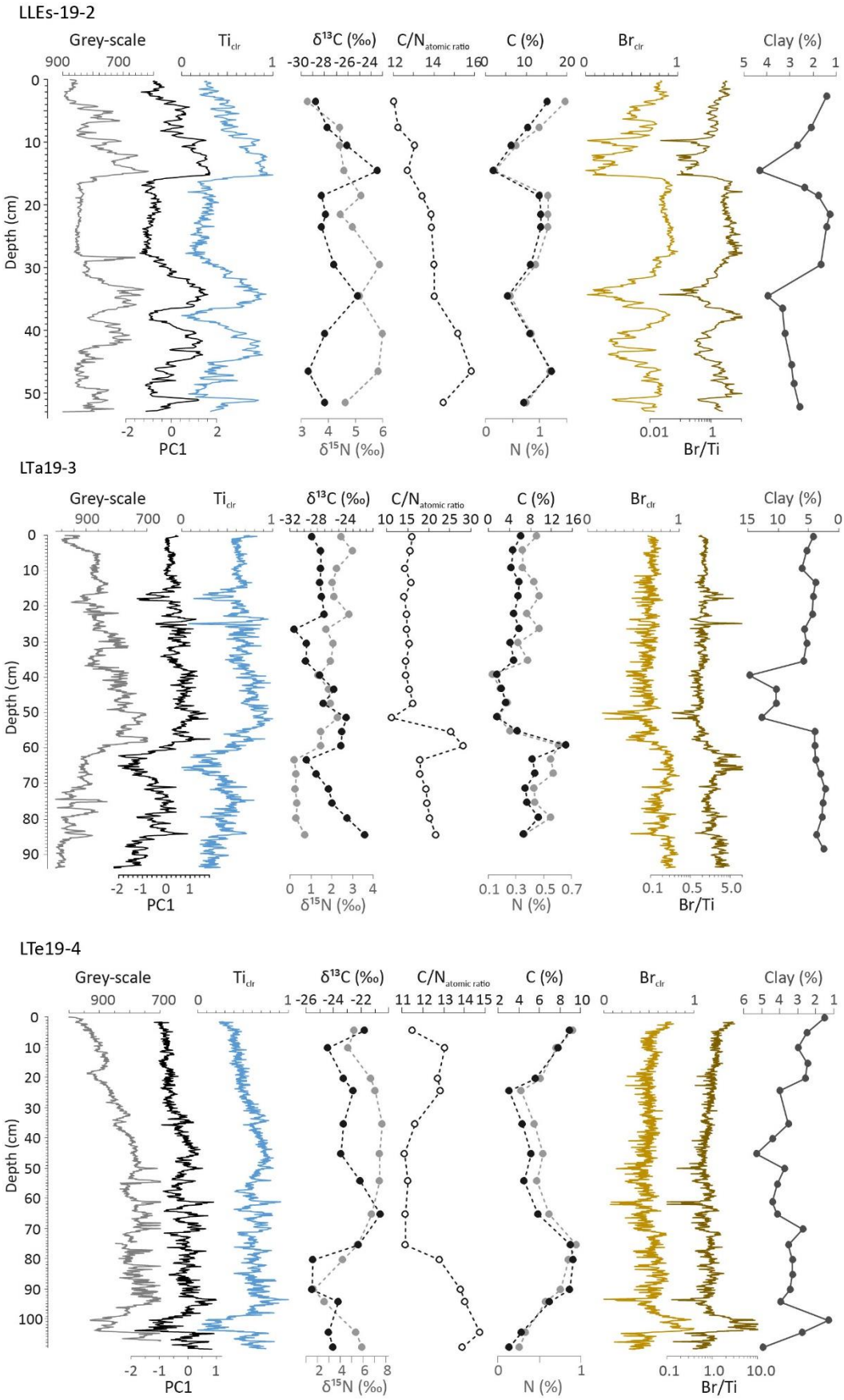
LLEs-19-2
Grey-scale
Ti clr
δ13C (‰)
C/N atomic ratio
C (%)
Br clr
Clay (%)
Depth (cm)
PC1
δ15N (‰)
N (%)
Br/Ti
LTa19-3
Grey-scale
Ti clr
δ13C (‰)
C/N atomic ratio
C (%)
Br clr
Clay (%)
Depth (cm)
PC1
δ15N (‰)
N (%)
Br/Ti
LTe19-4
Grey-scale
Ti clr
δ13C (‰)
C/N atomic ratio
C (%)
Br clr
Clay (%)
Depth (cm)
PC1
δ15N (‰)
N (%)
Br/Ti

**Figure 5**

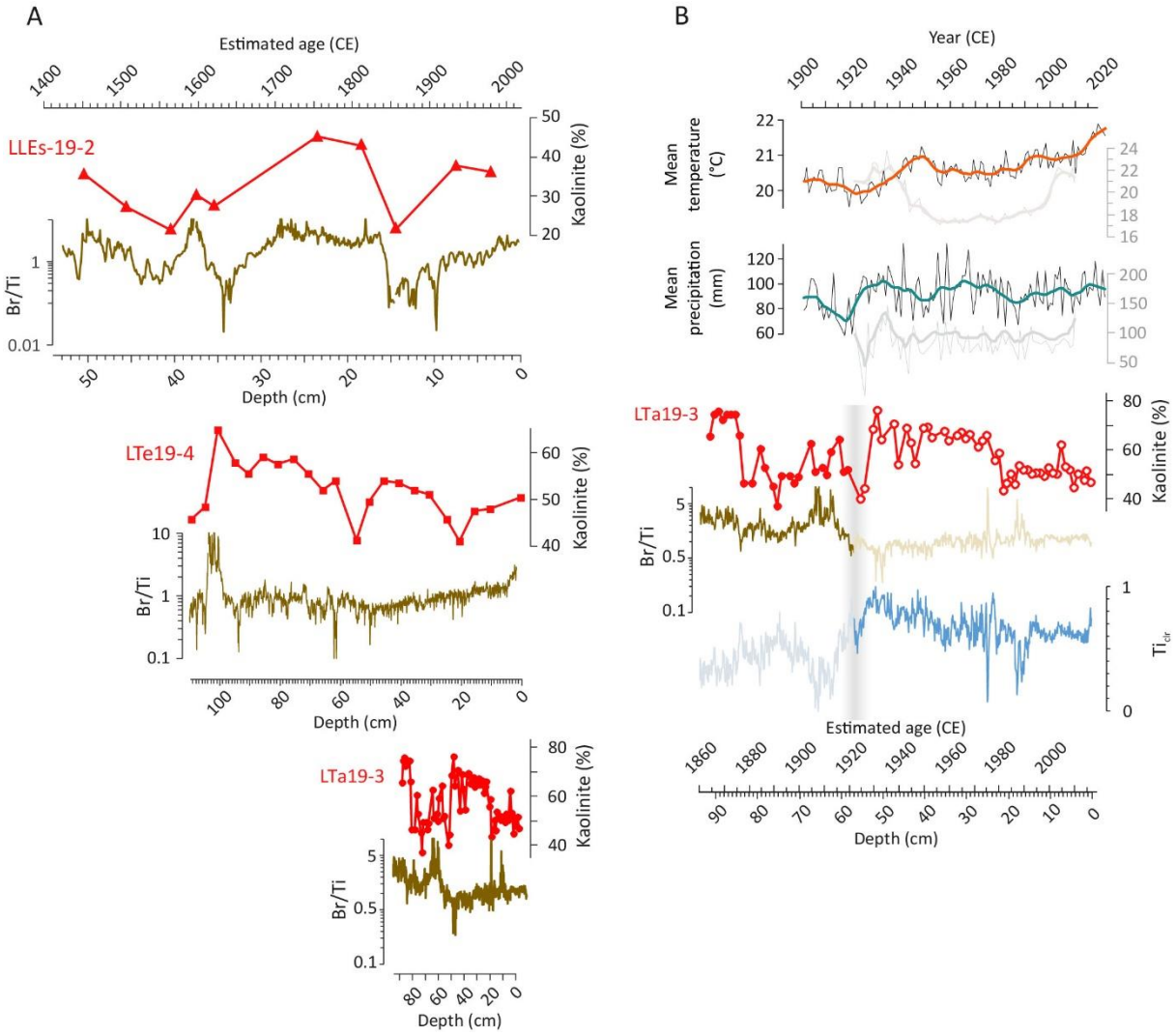


897

898 **Figure 6**